The Formation of Small-Scale Atmospheric Vortices via Baroclinic Horizontal Shearing Instability

MICHAEL S. BUBAN

Cooperative Institute for Mesoscale Meteorological Studies, University of Oklahoma, and NOAA/OAR/National Severe Storms Laboratory, Norman, Oklahoma

CONRAD L. ZIEGLER

NOAA/National Severe Storms Laboratory, Norman, Oklahoma

(Manuscript received 24 December 2014, in final form 30 November 2015)

ABSTRACT

This study presents a series of idealized simulations that attempt to replicate shear zones typical of drylines and other near-surface boundaries in the presence of horizontal virtual density gradients. The series of dry simulations are initialized to contain a north–south-oriented potential temperature gradient collocated with a constant-vorticity shear zone and employ north–south periodic boundary conditions. In all simulations, the shear zones frontogenetically collapse as wavelike perturbations develop that eventually roll up into discrete vortices. Convergence associated with the developing solenoidally forced secondary vertical circulation induces an accumulative shear zone contraction, which in turn increases the vertical vorticity of both the shear zone and the intensifying vortices, owing primarily to stretching that is partially offset by tilting of the vertical vorticity into the horizontal by the secondary circulation. The simulated vortices bear strong morphological resemblance to vortices reported in many earlier laboratory and numerical studies. To assess hypothesized baroclinic effects on the instability mechanism, the present results are compared to a previous study of barotropic horizontal shearing instability (HSI). Linear theory has been modified for the baroclinic cases by introducing a parametric model of frontal contraction, according to which the growth rate expressions incorporate model-prescribed, continuously varying shear zone widths. This modified parametric model is found to provide excellent agreement with the growth rates computed from the present simulations, suggesting that HSI can be extended to the baroclinic shear zone cases to a very good approximation over a range of near-surface boundary types.

1. Introduction

High-resolution observations have revealed the presence of small-scale misocyclones (i.e., vortices ~1–4 km in diameter) along drylines (Pietrycha and Rasmussen 2004; Murphey et al. 2006; Marquis et al. 2007; Buban et al. 2007), cold fronts (Kawashima and Fujiyoshi 2005; Arnott et al. 2006), sea-breeze fronts (Atkins et al. 1995; Friedrich et al. 2005), atmospheric boundary layer (ABL) convergence lines (Crook et al. 1991), and other surface-based boundaries. These misovortices typically attain their maximum growth rates and intensities within the ABL portion of the boundaries in which they are embedded, and their boundary environments are often characterized by enhanced convergence, horizontal along-boundary wind shear, and horizontal virtual temperature or density gradients. It is, therefore, reasonable to hypothesize that the nature of the collocated horizontal gradients of virtual density and horizontal shear may influence the development of misocyclones embedded within surface-based boundaries. It has previously been hypothesized that misocyclones form along surface-based boundaries due to a horizontal shearing instability (HSI).

Although a range of laboratory and numerical experiments have previously been conducted to study the instability of parallel shear flows in which the shear is everywhere unidirectional [for literature reviews, see Lee and Wilhelmson (1997, hereafter referred to as LW97), Buban and Ziegler (2016, hereafter referred to

Corresponding author address: Dr. Michael S. Buban, Atmospheric Turbulence and Diffusion Division, NOAA/OAR/Air Resources Laboratory, 456 S. Illinois Ave., Oak Ridge, TN 37830. E-mail: Michael.buban@noaa.gov

DOI: 10.1175/JAS-D-14-0385.1

as BZ16), and Buban (2014, hereafter referred to as B14)], most of these studies that included horizontal shear neglected potential effects of density differences on the shearing instability. In all cases in which the direct, first-order physical impacts of density differences on shearing instability were examined, those effectively two-dimensional problems were posed within the vertical plane and uniformly assumed a stable thermal stratification. In other words, one fluid with a given velocity was overlaid above another fluid with a different velocity and higher density to produce a gravitationally stable system. In contrast, relatively few studies have treated the instability of parallel shear flows in which a shear zone is characterized by a predominantly horizontal shear collocated with a horizontal virtual density gradient. One notably exceptional study by LW97 numerically modeled an idealized storm outflow boundary that developed a horizontal shear juxtaposed with a horizontal temperature gradient and subsequently developed simulated misocyclones. They found that misocyclone structure and growth rates were sensitive to the imposed vertical shear by modifying the lobe and cleft instability leading to HSI. Kawashima (2011) found that HSI growth rates decrease with decreasing gradient-normal shear along a simulated cold-frontal rainband. Both studies concluded that HSI growth rates increase with increasing horizontal shear.

In the limiting case where the virtual density difference across a surface-based boundary vanishes, this manifestation of HSI is barotropic in nature. Thus, in the barotropic case, linear theory can straightforwardly be applied. Indeed, it has been shown that HSI adequately explains the development of misocyclones along shear zones with characteristic scales of atmospheric boundaries in the barotropic limit (BZ16; B14). In the real atmosphere, varying scales and magnitudes of virtual density gradients and horizontal wind shears may occur along surface-based boundaries. The primary goal of the present study is to explore the effects of virtual density gradients on the HSI mechanism for misocyclone formation via a series of idealized baroclinic simulations featuring the superposition of a horizontal virtual potential temperature gradient within the horizontal shear zone. The introduction of a horizontal virtual density gradient causes the shear zones to frontogenetically contract, thus introducing a time variation to the HSI that has not been previously addressed. Although the present idealized baroclinic simulation results are hypothesized to be applicable to surface-based boundaries generally, the area of parameter space represented by the chosen initial conditions of the present study is particularly representative of drylines (e.g., Buban et al. 2012). The present study thus complements and extends the results of another study of the barotropic HSI mechanism reported by BZ16.

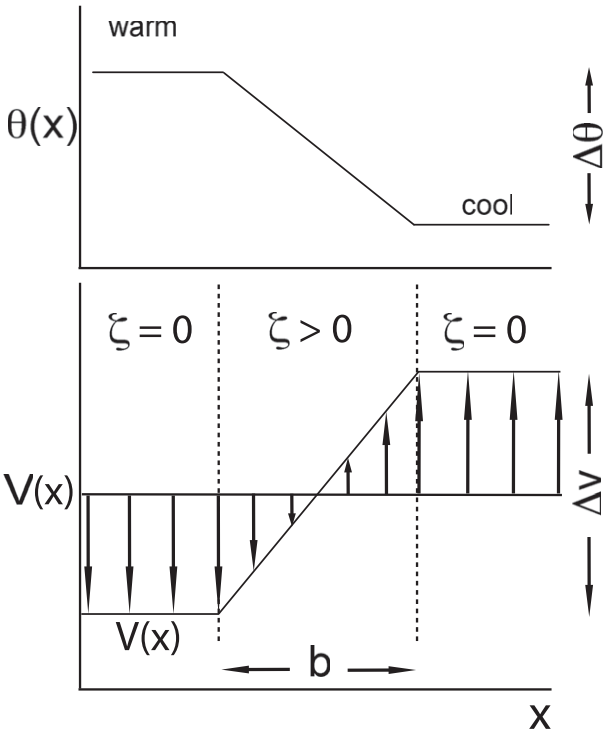

FIG. 1. Schematic setup of the idealized simulations. All symbols are defined in the text, and "b" is the shear zone width in Eq. (3).

2. Numerical methods

a. Model description

The simulations in the present study are conducted using the Collaborative Model for Multiscale Atmospheric Simulation (COMMAS; Wicker and Wilhelmson 1995; Coniglio et al. 2006; Mansell et al. 2010; Buban et al. 2012; BZ16). COMMAS is cloud resolving and nonhydrostatic, and its application in the present study includes a weakly diffusive fifth-order advection scheme (Wicker and Skamarock 2002). All explicit mixing terms have been deactivated in the simulations. The lower boundary has been treated as free slip while the upper boundary is assumed to be rigid.

The base-state flow and the shear zone in these idealized simulations are assumed to be meridionally oriented and centered within the model domain (Fig. 1). The simulations are run with periodic north–south boundary conditions and thus yield an essentially infinite-length channel. The simulation domain is configured with a grid spacing $\Delta x = \Delta y = \Delta z = 100$ m in the horizontal and vertical directions. The domain size is 29.9 km in the meridional direction (alongstream),

14.9 km in the zonal direction (cross stream), and 4 km in the vertical (i.e., $300 \times 150 \times 41$ grid points), while the time step is 2 s. As inferred from simulation results to be presented (and as implied by results of BZ16), the chosen grid spacing is hypothesized to adequately resolve commonly observed dryline features (e.g., shear zone width, vertical vorticity bands, and isolated misovortices and updrafts) as well as the physical instability mechanisms leading to dryline misovortex genesis.

The initial conditions for the simulations are produced by parametrically prescribing model variable fields. The idealized simulations will be referred to as ''baroclinic'' since they include a potential temperature gradient. All cases will hereafter be referred to via an acronym convention (e.g., case ''bc8m20s,'' where ''bc'' denotes baroclinic, ''8m'' denotes a shear zone width of 800 m, and ''20s'' denotes a 20 m s^{-1} shear). Since the present simulations are dry (i.e., no water vapor or cloud processes), the baroclinic zone is characterized by the horizontal potential temperature difference $\Delta\theta$. Results from the alternate moist case are theoretically identical to the present dry case (except for secondary effects of clouds) if the virtual potential temperature difference $\Delta\theta_v = \Delta\theta$. The vertical velocity (i.e., the ''w component'') is assumed initially to be zero everywhere. The 3D meridional component (v component) velocity field is prescribed with a constant value on the west side of the domain, a constant shear zone in the center of the domain featuring a linearly increasing v component in the x direction, and a constant value on the east side of the domain.

To simulate the dryline environment, a horizontal potential temperature difference of $\Delta\theta$ equal to 0.5 K is prescribed (with θ decreasing linearly from west to east across the shear zone). Both the $\Delta\theta$ value of 0.5 K and the range of widths of the temperature gradients (i.e., from 400 to 1000 m) are broadly representative of observed drylines (e.g., Ziegler and Hane 1993; Ziegler et al. 2007; Buban et al. 2007; Miao and Geerts 2007). The θ gradient is only imposed from the surface up to 1.5 km. Above 1.5 km, the initial conditions are horizontally homogeneous in all variables except for the v-component velocity. The basic stratification in all cases is neutral ($\theta = 300.5$ K).

Prior to BZ16 and the present study, the hypothesis that the HSI process could produce misocyclones had not been demonstrated conclusively for the case of drylines. The basic philosophy of BZ16 and the present study is to impose initial model conditions that are as consistent as feasible to the original assumptions of Rayleigh (1879)—only relaxing this similitude as necessary. Thus, BZ16 (and for consistency the present study as well) exclude vertical base-state shear effects by extending the Rayleigh-assumed 2D shear zone vertically through the domain depth.

Because of the inclusion of the horizontal θ gradient (thus, also a density gradient) and also to approximately counteract the intrinsic easterly density current phase speed, a westerly zonal u component is initially prescribed to the west of the dryline with a maximum value near the surface that linearly decreases to zero at 1.5 km. The initial westerly u component takes the parametric form $U(z) = U_{\rm sfc}[1 - (z/H)]$, where $U_{\rm sfc}$ (m s^{-1}) is the initial surface u component, z is the height (AGL), and H is the depth of the cold layer (1.5 km). Note that a consequence of imposing this vertical profile that exactly matches the linear decreasing horizontal flow generated by the cool ABL is to keep the leading edge of the cool ABL vertically erect. This in turn allows us to compare to the barotropic cases where the shear zone boundaries were vertical planes.

The theoretical ground-relative density current speed depends on the magnitude of the horizontal temperature gradient following the expression (Ziegler et al. 2010)

$$U_{\rm dc} = b_{\rm sf} U_{\rm sfc} - F\left(\frac{gD\Delta\theta}{\theta_0}\right)^{1/2} = 0, \qquad (1)$$

where $U_{\rm dc}$ is the zero net density current speed, $U_{\rm sfc}$ is the surface value of the environmental flow (4.5 m s^{-1}), θ replaces θ_v in the present dry case, $b_{\rm sf}$ is a constant that takes into account surface friction and is set to unity in the present study, F is a Froude number also set to unity, g is the gravitational acceleration, and D is the density current depth (1.5 km). The first and second right-hand-side terms in Eq. (1) are the boundary-normal effective environmental wind speed and the ground-relative density current speed, respectively.

After a short period of initial dynamical adjustment in which the intrinsic density current speed rapidly balances the environmental flow and the boundary width contracts via meridionally uniform frontogenetic forcing, the basic simulated flow structure follows the schematic shown in Fig. 1. Previous modeling studies have found that development of HSI can be sensitive to the vertical shear normal to the density current when the effects of either or both precipitation and surface friction were included (LW97; Kawashima 2011). To compare with BZ16, the only other effect to a purely barotropic HSI was the inclusion of a density gradient, while maintaining the same variations in horizontal shear and shear zone width among the various simulations. Any effect of vertical shear on HSI is beyond the scope of the present study.

The previously mentioned periodic north and south boundary conditions allow northward-moving features

TABLE 1. Magnitude of the uniform initial vertical vorticity ζ_0 ($\times 10^{-3}$) within the shear zone for each simulation.

	6 m s^{-1}	8 m s^{-1}	12 m s^{-1}	16 m s^{-1}	20 m s^{-1}	24 m s^{-1}
400 m	15	20	30	40	50	60
500 m	12	16	24	32	40	48
600 m		13.3	20	26.7	33.3	40
800 m			15	20	25	30
1000 m			12	16	20	24

to pass through the northern boundary and reenter the southern boundary to continue evolving. Wave-radiating boundary conditions are employed on the eastern and western lateral domain boundaries (e.g., Klemp and Wilhelmson 1978; Wicker and Wilhelmson 1995; Peckham and Wicker 2000), while a free-slip boundary condition is employed at the surface. Parameterized friction, surface fluxes, and radiation schemes are all deactivated in the simulations, since the goal of this study is to focus attention on horizontal shearing instability mechanisms.

To probe the hypothesized effects of an imposed baroclinic structure on the classical barotropic HSI mechanism, a series of simulations are conducted by varying the width of the shear zone and its magnitude across the shear zone in the presence of the imposed $\Delta\theta$ value—thus, covarying the magnitude of the initial vorticity and θ gradient within the shear zone (Table 1). A random v-component perturbation of 0.01 m s^{-1} is also added to the initial wind field. It is noted that sensitivity tests that have either varied the x dimension of the model domain or imposed a sinusoidal initial v-component perturbation with random amplitude and phase in the y direction (B14) essentially reproduce the results of the present study.

b. Spectral density estimation

To quantify the characteristics of the instabilities developing in the idealized simulations, spectral density estimation is performed on spatial series within the shear zone in the meridional or downstream direction (BZ16) at $z = 250$ m. Since the vorticity is zero outside the shear zone and a positive constant within the shear zone, going from west to east across the shear zone, a positive jump is seen on the western edge of the shear zone with a negative jump on the eastern edge. By computing the change in vorticity between grid points and averaging in the downstream direction, eastern and western edges of the shear zone are found as a function of time. The spectral density estimate is computed by taking the Fourier transform of the windowed autocorrelation function, providing the smoothed variance of a variable as a function of wavenumber. The spectral density estimation follows the smoothed autospectral procedures described by Jenkins and Watts (1969, hereafter referred to as JW69). The amplitude spectra displayed in the current study are derived from the square root of the variance spectrum.

The evolving spatial series of variables (e.g., u, v, and vertical vorticity ζ) are output in the downstream direction within the shear zone of each simulation. The mean values of each variable are computed and subtracted from each detrended series, the autocovariance functions are computed, and a lag (Tukey) window is applied to calculate the resulting smoothed spectral estimates. Finally, spectral estimates are averaged over wavenumber space. Since the velocity variance is distributed over a continuous range of wavenumbers in a plot of spectral velocity variance density estimates, the area under the spectrum is equal to the percentage of the velocity variance of the series that is explained by the wavenumbers in the range from k to $k + \Delta k$. For convenience in subsequently comparing spectral evolution to vortex shear amplitude, the square root of the velocity variance is instead displayed in all spectral plots.

It is necessary to model a ground-relative quasi-stationary dryline shear zone to directly relate the smoothed autospectral evolution to misocyclone intensification via autospectral calculations along fixed values of the y coordinate (i.e., along dryline). Increasing vertical shear of the dryline-normal component generally forces the initially cool, moist ABL to be shallower and warmer while inducing movement of the dryline in the direction of the shear (e.g., Peckham and Wicker 2000). Thus, introducing vertical shear in the present study would prevent the necessary ability to control the parameters for depth and magnitude of the temperature difference and result in a simulated ground-relative dryline movement, which in turn would prevent proper calculation and interpretation of autospectral evolution. Therefore, as previously discussed, including vertical shear other than necessary to cancel intrinsic density current motion is considered beyond the scope of the present study.

3. Results

The series of idealized dry baroclinic simulations assume initial shear and width parameter values that are characterized according to each shear zone's vertical vorticity value (Table 1). All simulations have a similar general evolution typified by contraction of the shear zone widths to about 2–3 times the grid spacing before periodic disturbances grow and distort the shear zone in a wavelike manner. The resulting waves roll up into discrete vortices that persist for a brief time, before nonlinear processes lead to vortex mergers and evolution

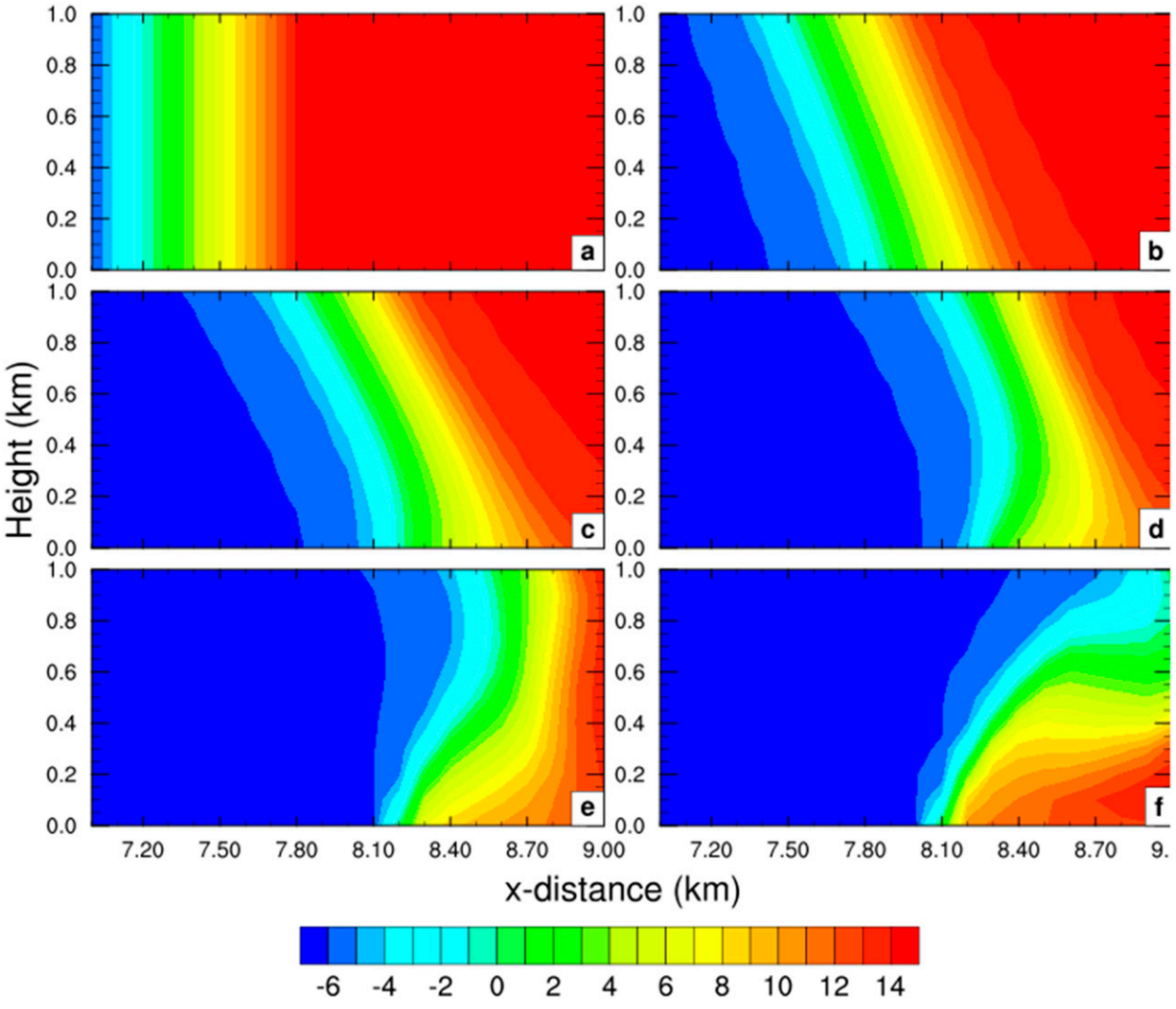

FIG. 2. Evolution of the color-filled v-component field (m s^{-1}) in the shear zone in an x–z cross section at (a) 0, (b) 120, (c) 240, (d) 360, (e) 480, and (f) 600 s in the bc8m20s simulation. Positive values represent flow directed into the page. The shear zone initially shifts eastward and rotates counterclockwise due to the ambient westerly velocity that decreases with height, then rapidly stabilizes as the solenoidally induced secondary circulation intensifies. The initial linear surface wind profile is shifted eastward and slightly sharpened due to convergent accumulation.

into turbulence. On the other hand, there are also somewhat minor differences among the various simulations in terms of detailed characteristics such as the vortex growth rates, the number and sizes of vortices, and how fast the shear zone contracts. Despite the frontal collapse of initial shear zones in the baroclinic cases, the results can usefully be generalized in similar fashion to the barotropic cases reported by BZ16 in which the initial shear zone was steady.

Two cases that typify the results among all the simulations will subsequently be examined in more detail. These two cases were chosen because their barotropic counterparts (i.e., simulations with the same shear and shear zone widths, but with constant density) were examined in detail in a previous study (BZ16), thus facilitating comparison with the present study.

a. Early shear zone evolution

The initial collapse of the shear layer in the bc8m20s case as visualized via the evolving v-component velocity profiles at several times prior to the emergence of discrete vortices (Fig. 2) is similar in all simulations. The shear layer has an initial eastward motion before slowing and becoming essentially stationary. The shear zone width initially decreases as it decelerates, although the contraction is greater on the western side of the shear zone than on its eastern side. Immediately prior to the emergence of the vortices, approximately 75% of the

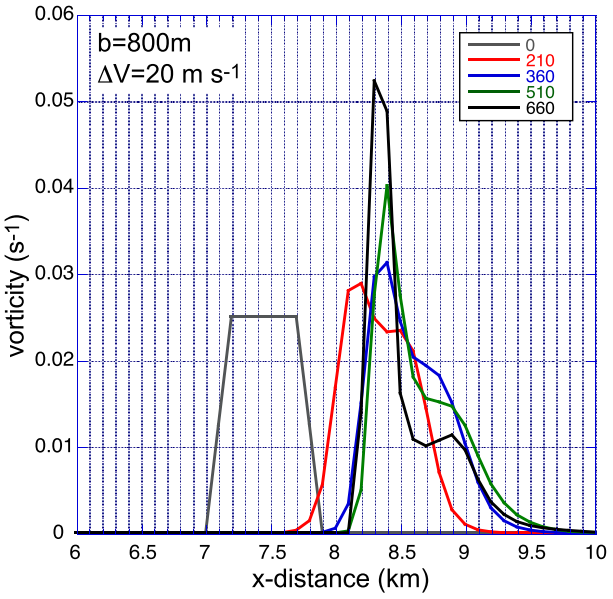

FIG. 3. Evolution of the shear zone vorticity at $z = 250$ m. The colored curves are the vertical vorticity profiles at different times (s; after start of simulation) for the bc8m20s case.

shear is located within an east–west distance interval of less than 2Δ on the western edge of the shear zone. In the vertical, the shear zone width contracts at about the same rate from the surface to ~300 m with a slightly slower rate near the top of the density current where the convergence is slightly less and the shear zone is wider.

The peak vorticity values increase as time progresses (Fig. 3), and the distance interval containing these higher values also decreases (i.e., evolution from a top hat profile to a steep single-peak profile). During shear zone contraction, the distance containing lower vorticity values actually increases. The vorticity gradient is largest on the western side of the shear zone, and gradually weakens from west to east. The vorticity profile just before the appearance of discrete vortices is characterized by a rapid increase in vorticity on the western shear zone edge, followed by a peak in vorticity and a gradual exponential-like decrease in vorticity continuing to the east. This initial evolution of the shear zone is consistent with baroclinically forced frontal collapse accompanied by accumulation of the v-component velocity shear (e.g., Ziegler et al. 1995). In the vertical, the vorticity values are largest at lower levels and decrease near the top of the density current consistent with a slightly wider shear zone.

It is hypothesized that stretching and tilting of the initially vertical shear zone vortex lines by the solenoidally induced, frontogenetic secondary circulation importantly augments the circulation of the shear zone, in contrast to the barotropic case wherein the circulation is conserved. The hypothesized vorticity intensification potentially augments the shear available to the growing HSI-induced misocyclones. The evolution of the peak vorticity within the initially contracting shear zone can usefully be approximated in terms of the predominant vorticity tendencies due to stretching and tilting. Since the shear zone is contracting, one would expect the magnitude of the peak vorticity to increase due to stretching. The vertical vorticity equation can be written neglecting y variations in the following form:

$$\frac{D\zeta}{Dt} = -\zeta\frac{\partial u}{\partial x} - \frac{\partial v}{\partial z}\frac{\partial w}{\partial x}, \tag{2}$$

where effects of friction and the earth's rotation have been neglected. The first right-hand-side term in Eq. (2) is the vorticity tendency stretching term, while the second term is the tilting term. Since the variables are averaged in the y direction (i.e., all variations are in the x–z plane), the solenoidal term does not appear in Eq. (2). Taking averages of the simulated vorticity in each north–south grid column, the maximum average vorticity value in the east–west direction (i.e., the peak in the curves in Fig. 3) is obtained at each time. The expected peak vorticity value may then be estimated given an initial vorticity value (i.e., the constant barotropic value) plus a change due to the presence of stretching and tilting. For the stretching term, the peak vorticity value (i.e., ζ) is determined and the divergence ($\partial u/\partial x$) is calculated to compute a vorticity tendency at that location and time. An analogous approach is followed to compute the tilting term.

Both the stretching and tilting terms are initially very small as the model is adjusting to the initial conditions until about 200–300 s. After 300 s, the stretching term begins to increase exponentially. The tilting term increases slowly, initially with positive tendency values, and then decreases more rapidly with negative values ensuing after 500 s. To see the net effect on the resulting vorticity evolution, the tendency values are multiplied by the time interval between calculations and added to the previous estimated vorticity values. In this manner, the discrete form of the vorticity equation [Eq. (1)] is integrated from some initial time to some later time. The net result is an exponential increase of the estimated vertical vorticity, with values that are close to what was output from the simulations, although the actual simulated values are slightly higher at early times (until about 300–400 s) and somewhat lower after 400 s (Fig. 4). If considering only the initial vorticity and the stretching term (green triangles in Fig. 4), the estimated vorticity overestimates the actual vorticity. The tilting term,

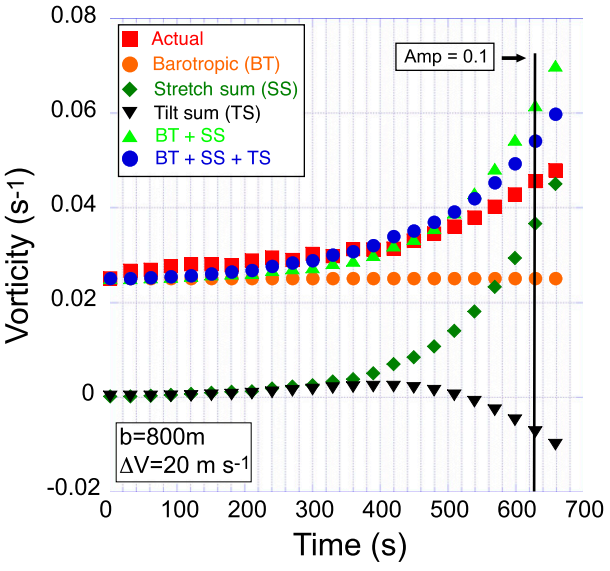

FIG. 4. Vertical vorticity values at various times for the bc8m20s case. Actual vorticity from the simulation (red squares); initial vorticity (orange circles); integrated stretching component to the total vorticity (green diamonds); integrated tilting component to the total vorticity (inverted black triangles); the sum of the initial and stretching integrated vorticity (green triangles); and sum of the initial, stretching, and integrated tilting vorticity (blue circles).

however, compensates by redistributing vertical vorticity into horizontal vorticity at later times. The sum of the tilting and stretching terms added to the initial vorticity thus yields a good estimate of the vorticity at early times. Note that at later times, the estimated and actual vorticity values begin to diverge with the estimated values greater than actual values. At these later times, the shear zone width is nearing 2–3 times the grid spacing, implying that the simulation is unable to increase the vorticity as fast as the calculated stretching and tilting terms would suggest.

b. *Emergence of shear zone instability*

Waves emerge along the nearly stationary shear zone as seen in the v-component wind fields by 840 s in the bc5m16s case (Fig. 5). By this time, the perturbations along the shear zone have grown by two to three orders of magnitude from the initial random perturbation. As time progresses, a series of waves continue to grow exponentially, however, the waves are not equally spaced and have north–south variation in their amplitudes. As the simulation proceeds into the nonlinear regime, the perturbations continue to grow and begin to roll up into discrete vortices with varying sizes and spacing. This process can more readily be seen in the vertical vorticity fields (Fig. 6). Initially, wavelike vorticity perturbations emerge and grow exponentially in time. The wavelike vorticity perturbations begin to contract into cores and increase in magnitude as the discrete vortices start to form. As in the v-component wind fields, a complex structure is seen with evidence of vortex mergers by 1140 s into the simulation.

In comparison to the bc5m16s case, the shear zone for the bc8m20s case is characterized by the emergence of small-amplitude waves by ~1080 s into the simulation (Fig. 7). These waves continue to grow in amplitude and eventually roll up into discrete vortices with various wavelengths and amplitudes by ~1200 s. The vorticity fields also behave similarly in the bc8m20s case as in the bc5m16s case, with wavelike perturbations evolving into discrete vortices with varying amplitudes and wavelengths that begin merging by ~1320 s (Fig. 8).

c. *Perturbation wavelengths*

There is a question as to what degree linear theory can be applied to cases where there is a density gradient present. In contrast to the case of barotropic (constant width) shear zones, in the baroclinic cases there is a background u-component wind and a corresponding horizontal convergence that frontogenetically forces a time-dependent width of the resulting shear zone. In all baroclinic simulations, the shear zone width collapses to ~2–3 times the grid spacing prior to the emergence of significant wave amplitudes. Perhaps it could be expected that at least some component of the resulting growth rates would reside around the wavelength at which linear theory would predict the maximum to occur given a shear zone width of ~2–3Δ.

Spectral density estimates at successive times show the perturbation amplitude evolution as a function of wavenumber for the bc5m16s case (Fig. 9). Assuming a shear zone width of 2–3Δ, linear theory predicts the most unstable wavenumbers to be in the range of 12.6–19 (λ = 2370–1580 m). From the start of the simulation, all wavenumbers begin to grow and there is very little difference in the amplitudes among the wavenumbers. By 600 s into the simulation, structure in the spectral density estimate begins to emerge with a maximum in amplitude around wavenumber 12. This peak in amplitude grows exponentially and remains the peak as discrete vortices emerge. Also, this simulation features a main peak and additional peaks in the spectrum. The main peak in amplitude (κ = 12.0, λ = 2490 m) is close to the peak in amplitude expected to emerge by growth of the theoretical most unstable mode assuming an initial shear zone of ~3Δ (κ = 12.6, λ = 2370 m). In addition to the primary peak, a secondary maximum occur around wavenumbers 6–7 (λ = 4980–4270 m) and 24–26 (λ = 1150–1250 m). The additional peaks occur at nearly one-half and twice the wavenumber of the primary peak in amplitude, suggesting that a possible resonant

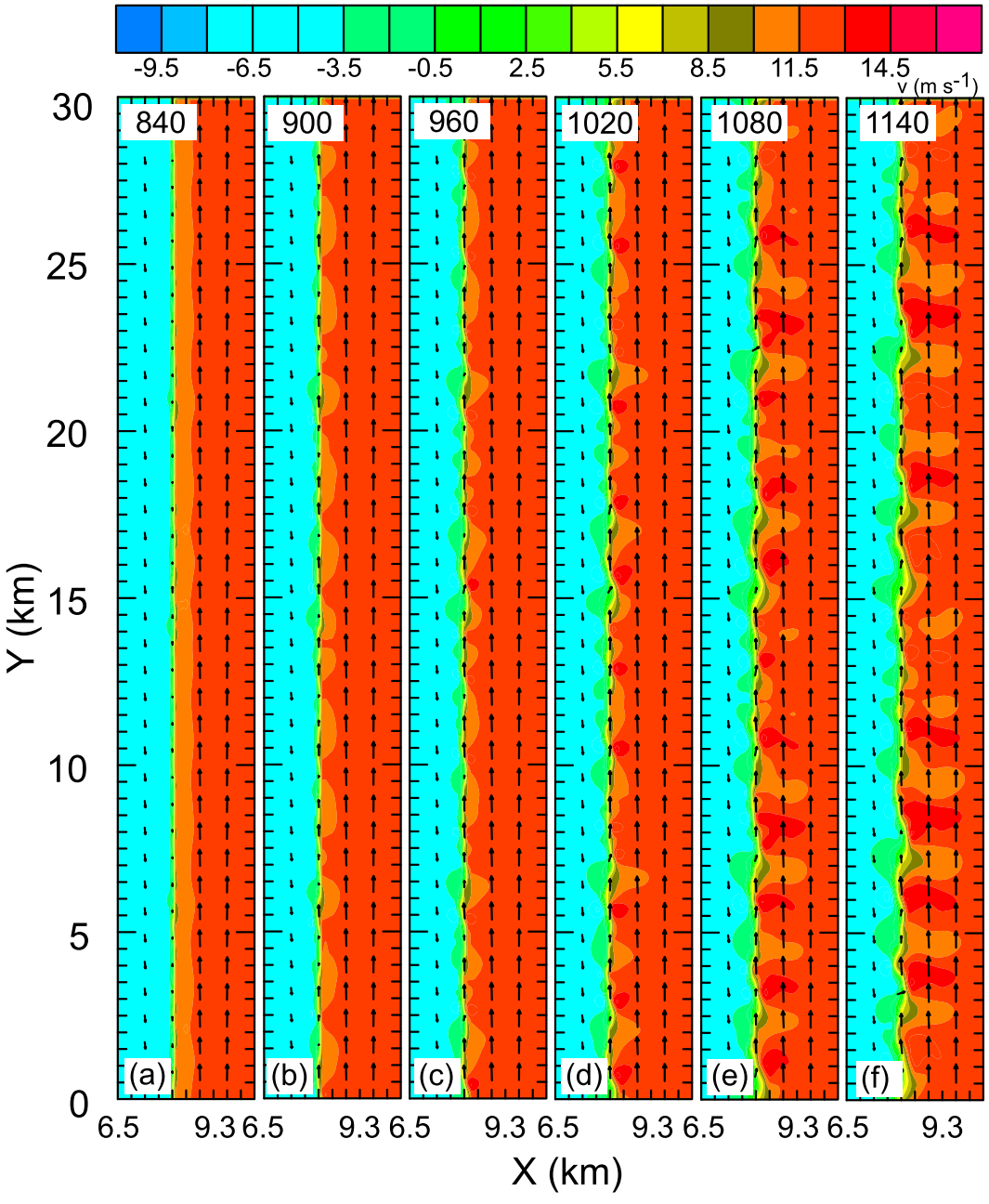

FIG. 5. Fields of v-component wind (color filled) and horizontal wind vectors (500 m = 8 m s^{-1}) for the bc5m16s case at the second model level (z = 150 m): (a) 840, (b) 900, (c) 960, (d) 1020, (e) 1080, and (f) 1140 s.

interaction is modulating the magnitudes of the secondary peaks.

The main peak in the spectrum is found around wavenumber 16 (λ = 1870 m) in case bc8m20s (Fig. 10). This peak in amplitude is close to the peak in amplitude expected to emerge by growth of the theoretical most unstable mode assuming an initial shear zone of ~2.4Δ. As in the bc5m16s case, the bc8m20s case contains a main peak in amplitude as well as two smaller secondary peaks in amplitude around wavenumbers 25–26 (λ = 1200–1150 m) and wavenumbers 10–11 (λ = 2990–2720 m). Note that the growth rate of the main peak is smaller and that the small-wavenumber growth rate is larger than in the bc5m16s case. This is due to the combination of a larger shear zone width and a weaker shear zone vorticity in the bc8m20s case.

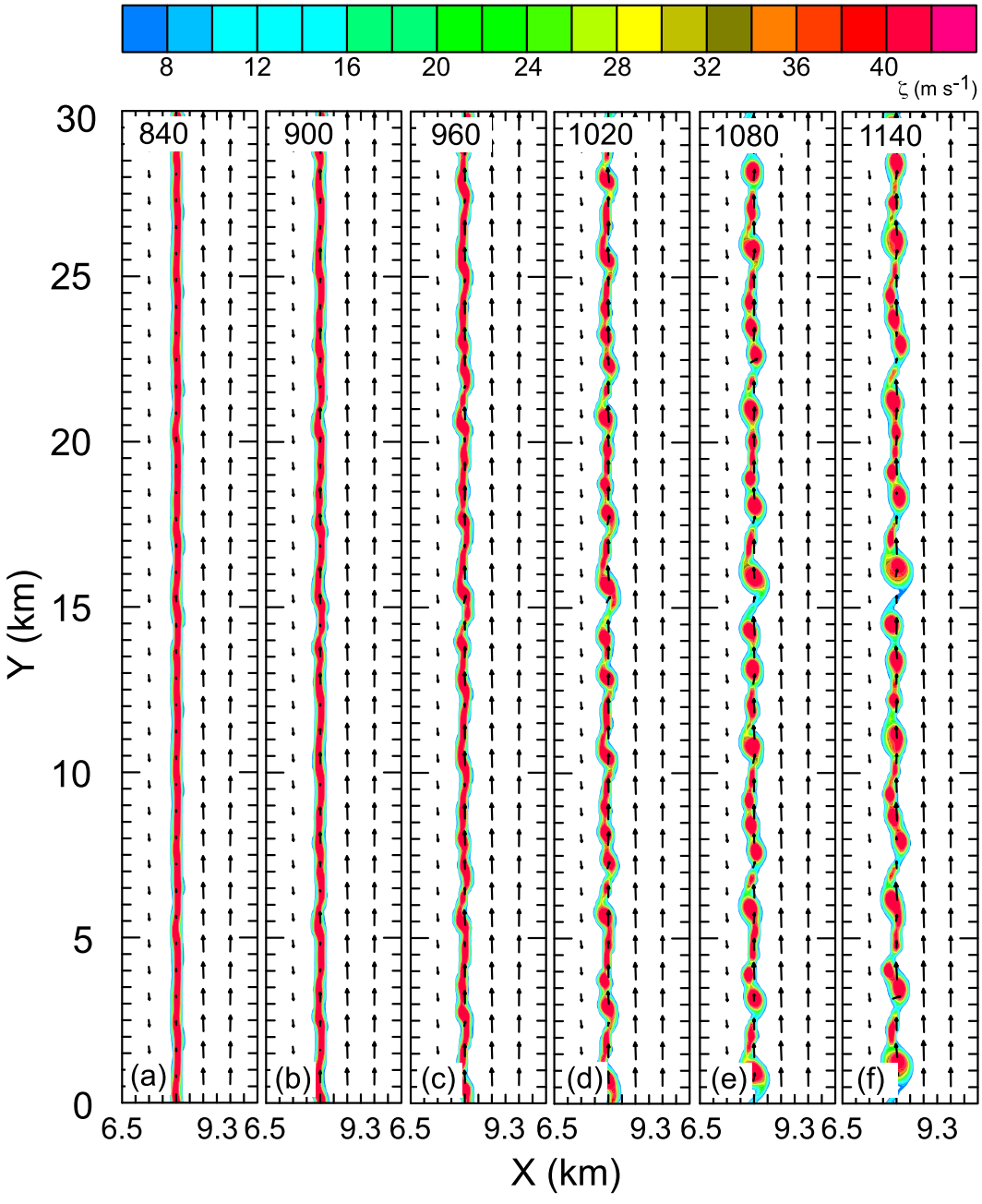

FIG. 6. Vertical vorticity (color filled) and horizontal wind vectors (500 m = 8 m s^{-1}) for the bc5m16s case at the second model level (z = 150 m): (a) 840, (b) 900, (c) 960, (d) 1020, (e) 1080, and (f) 1140 s.

d. Perturbation growth rates

The growth rates in the simulations can be computed from the spectral density estimates. However, the growth rates are not constant in the baroclinic cases, but instead increase with time as the shear zone contracts. By plotting the perturbation amplitude as a function of time on a semilog graph, it may be seen that the time series curve upward slightly thus implying increasing exponential growth with time (not shown).

It is useful to determine if linear theory may be applied to the baroclinic cases despite the complication imposed by the time-varying shear zone width. The evolution of the shear zone width may be parametrically approximated by computing the maximum shear zone vorticity as proxy for the shear zone width

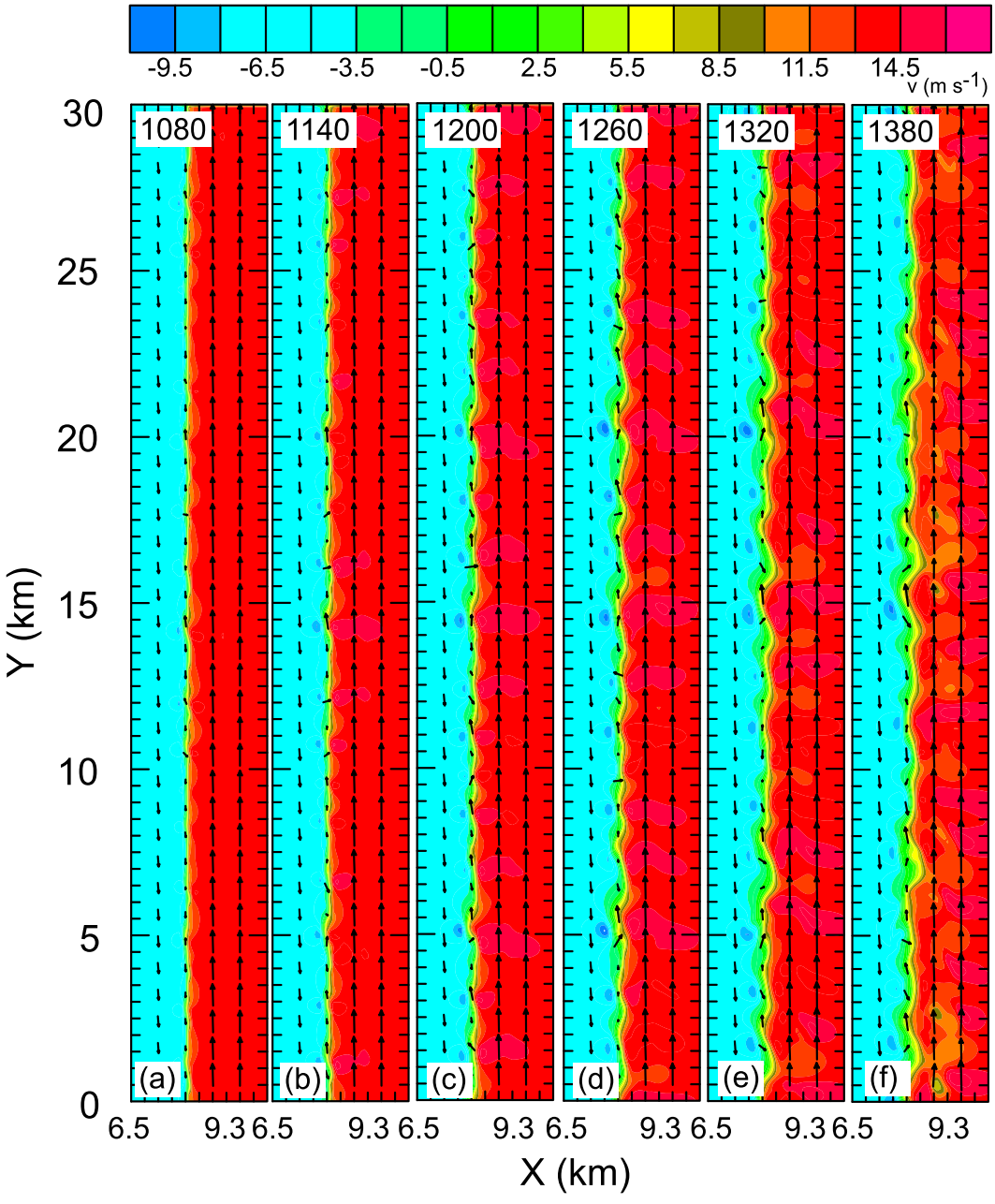

FIG. 7. Fields of v-component wind (color filled) and horizontal wind vectors (500 m = 8 m s^{-1}) for the bc8m20s case at the second model level (z = 150 m): (a) 1080, (b) 1140, (c) 1200, (d) 1260, (e) 1320, and (f) 1380 s.

via the relationship $b = \Delta U/\zeta$ (where ΔU is nearly constant). Note that the variable b here and for the remainder of the paper is different than the variable b_{sf} in Eq. (1). The modeled shear zone vorticity evolution closely conforms to a tanh function in time (Fig. 11). The tanh function for $\zeta(t)$ takes the form $\zeta(t) = a\tanh(rt + m) + d$, where a is the vorticity amplitude; r is the shape parameter; and m and d are displacements in the x and y dimensions, respectively. An example of a tanh function that has been fitted to the model-output vorticity is shown in Fig. 11. The fitted tanh curves tend to follow the model output very closely in all cases, thus, providing an excellent parametric representation of the vorticity profile and, hence, also the shear zone width at any given time. Fitted tanh parameter values for the various simulations are listed in Table 2.

The growth rate from linear theory is proportional to the vorticity in the shear layer, the latter is typically assumed to

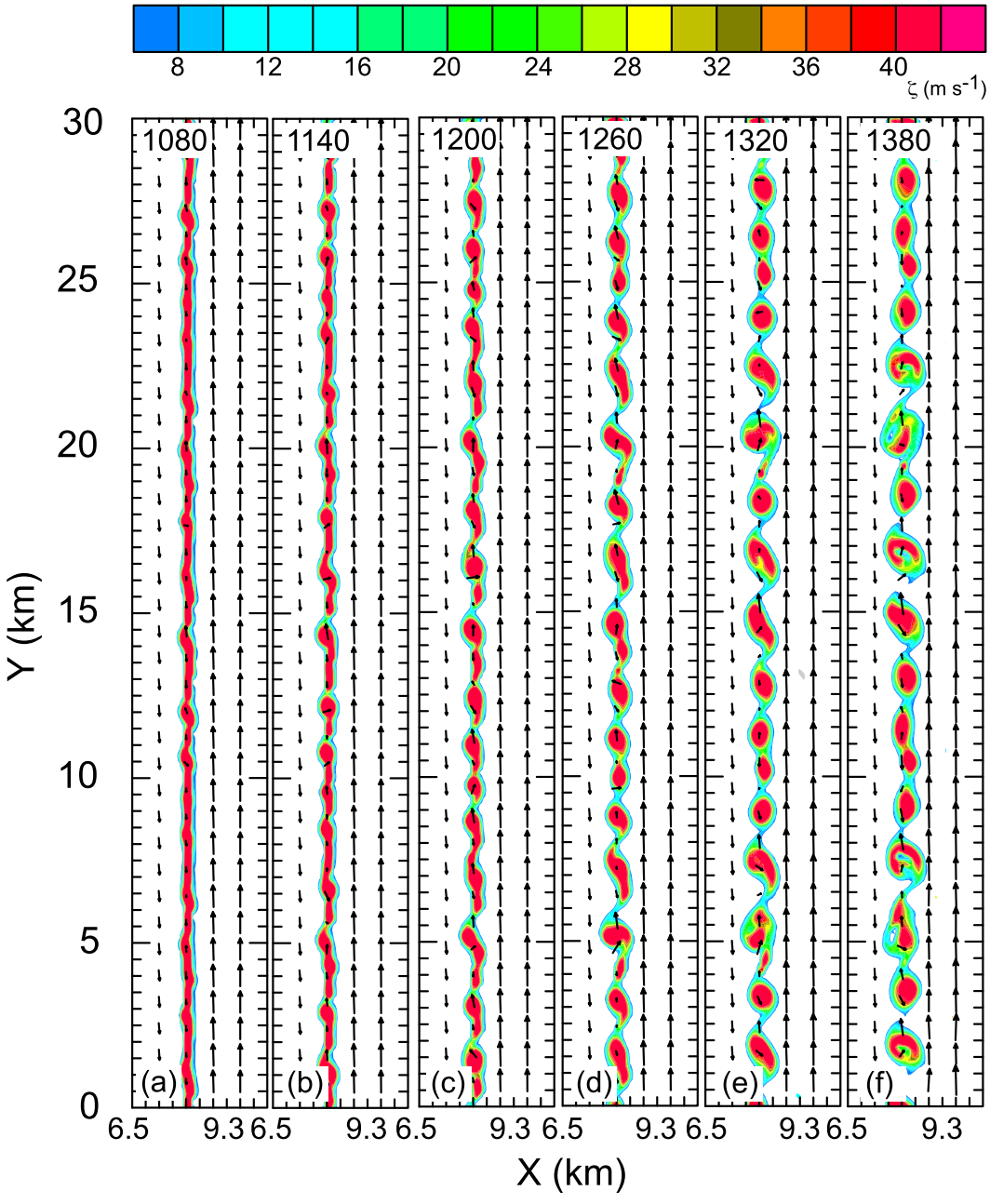

FIG. 8. Vertical vorticity (color filled) and horizontal wind vectors (500 m = 8 m s^{-1}) for the bc8m20s case at the second model level (z = 150 m): (a) 1080, (b) 1140, (c) 1200, (d) 1260, (e) 1320, and (f) 1380 s.

be constant as appropriate for the conventional barotropic base-state case (e.g., Rayleigh 1879; BZ16). The growth rate of barotropic HSI takes the following form:

$$c^2 = \frac{U^2}{b^2}[(kb-1)^2 - e^{-2kb}]. \quad (3)$$

Substituting a time-varying vorticity function into the expression for the HSI growth rate Eq. (3) allows us to model the total growth rate for the baroclinic cases. The maximum vorticity of each simulation is computed at each output time, and a hyperbolic-tangent function is then fitted to the maximum vorticity data using the Levenberg–Marquardt algorithm as implemented in the SciPy software package. Substituting the above analytic tanh functional expression for the vorticity into Eq. (3) yields the time-dependent growth rate as follows:

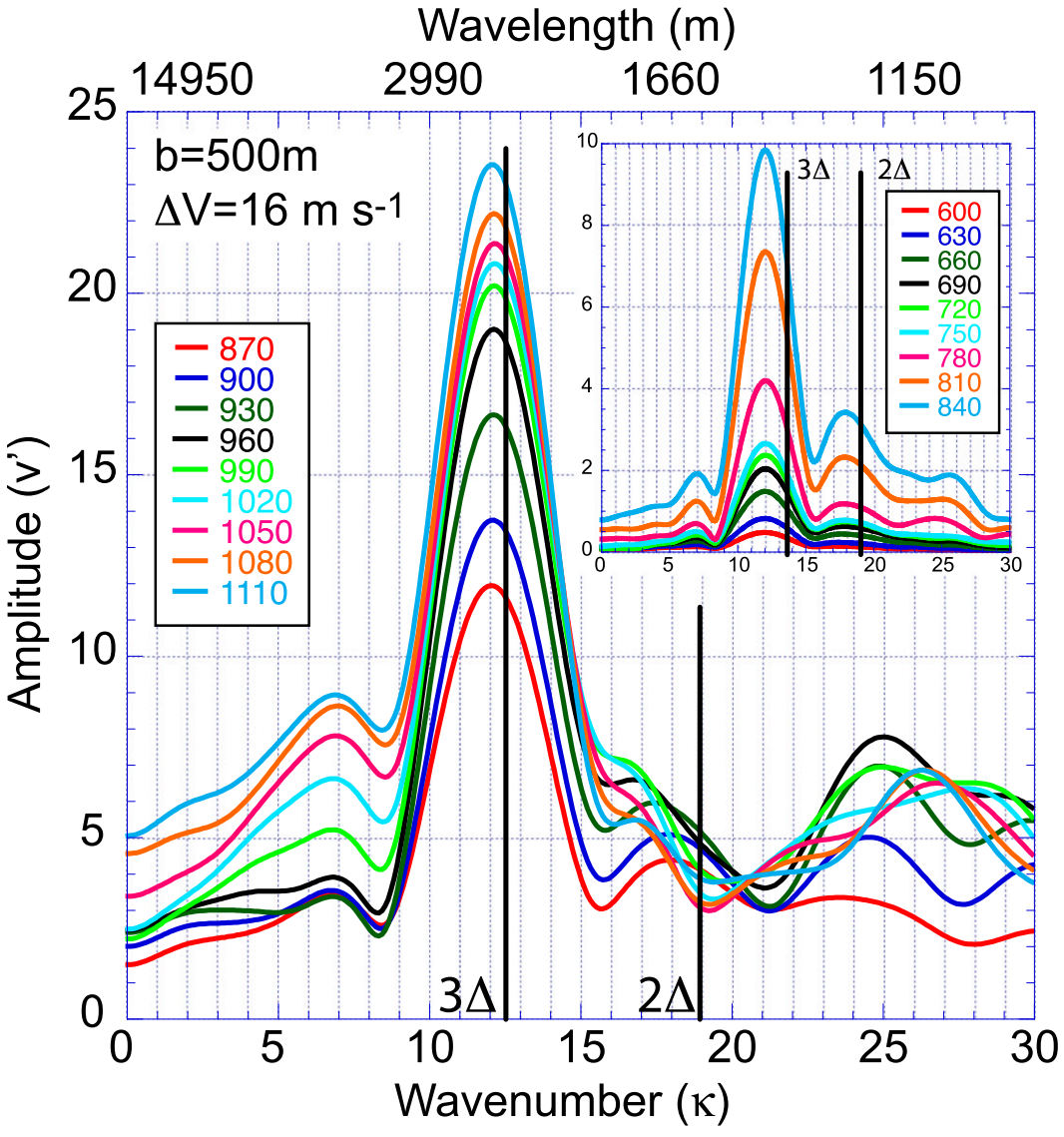

FIG. 9. Spectral density estimates of the v-component perturbation wind amplitude ($\mathrm{m\,s^{-1}}$) as a function of wavenumber during the periods of 870–1110 and 600–840 s (inset) after the start of simulation bc5m16s. The vertical black lines denote the most unstable wavenumbers predicted by linear theory for a shear zone width of 2Δ and 3Δ.

$$c(t) = \frac{a}{2}[\tanh(rt+m)+d]\left\{\left[\frac{2kU}{a\tanh(rt+m)+d}-1\right]^2 - \exp\left[\frac{-4kU}{a\tanh(rt+m)+d}\right]\right\}^{1/2}. \quad (4)$$

Although Eq. (4) represents an instantaneous growth rate, it is more physically relevant to compare average growth rates over a reasonable amount of time since growth rates require an arbitrary time interval to be computed from the model output.

Although the simulation model is predicting the local time-dependent growth rate, the detailed simulated local evolution is difficult to explain given the complex interaction of the local nonlinear terms. By averaging spatially in the y direction and in time permits the extraction of basic physical insight into why the model boundary behaves as it does. An average growth rate is obtained by performing quadrature of Eq. (4) over some time interval for comparison against the simulation data. To compute the corresponding average growth rate for the simulated shear zones, the local growth rate between two neighboring output intervals (i.e., the output

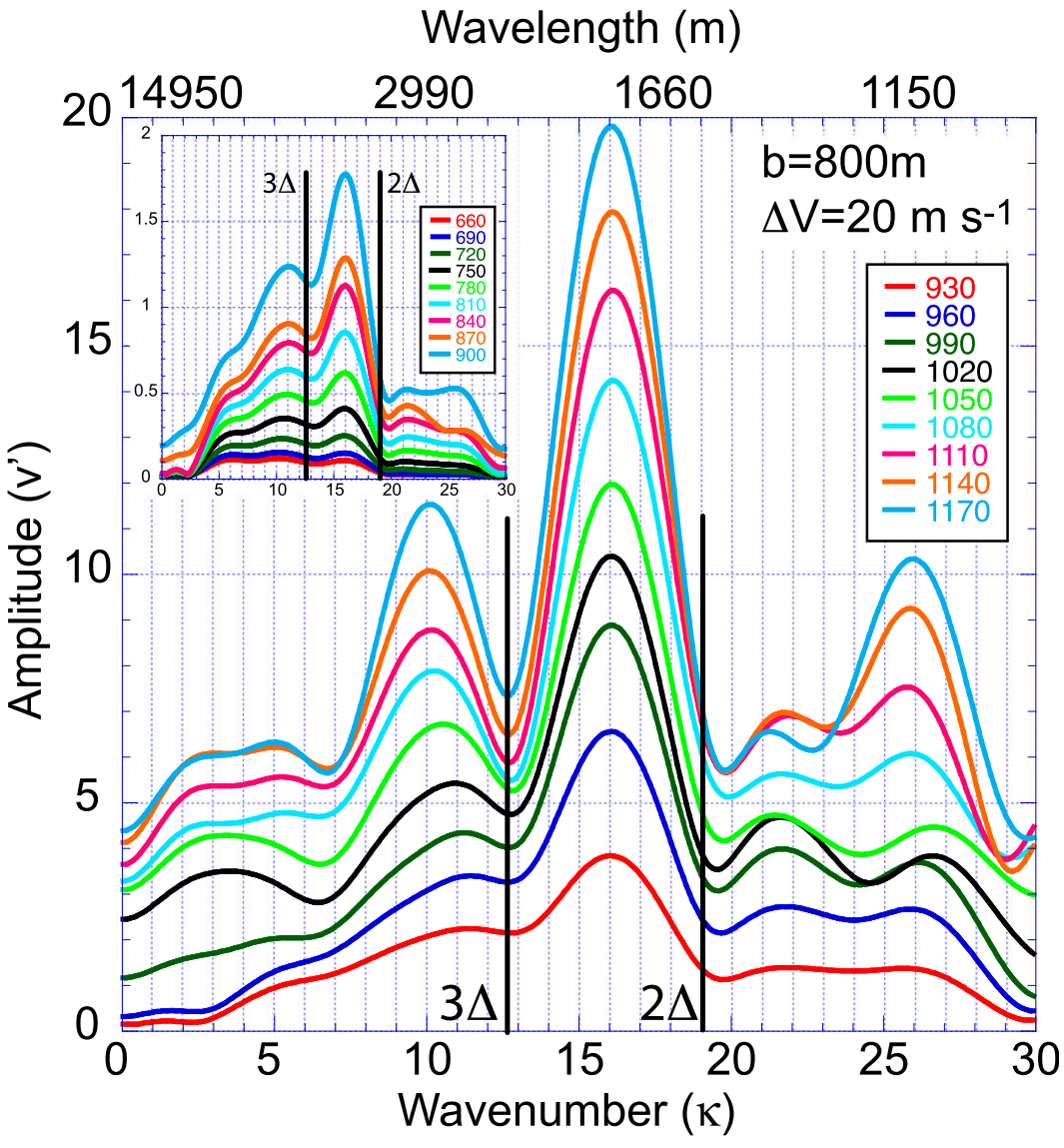

FIG. 10. Spectral density estimates of the v-component perturbation wind amplitude ($\mathrm{m\,s^{-1}}$) as a function of wavenumber during the periods of 930–1170 and 660–900 s (inset) after the start of simulation bc8m20s. The vertical black lines denote the most unstable wavenumbers predicted by linear theory for a shear zone width of 2Δ and 3Δ.

interval was 30 s in all simulations) is computed via the following expression:

$$c(t) = \frac{1}{\Delta t} \ln \left[\frac{C_{uu}(t)}{C_{uu}(t-1)} \right], \tag{5}$$

where C_{uu} is the spectral density estimate. The average growth rates from the parametric model and the simulations are then computed from Eqs. (4)–(5) via

$$c_{\mathrm{avg}} = \frac{1}{N} \sum_{i=1}^{N} c(t)_i, \tag{6}$$

where N is the same in the simulation calculations and the parametric model calculations. Results from the computed average growth rates from the simulations and the values computed from Eq. (4) are compared in Fig. 12. For the 1000-m runs (Fig. 12a), the growth rates are in good agreement between the parametric model and the calculated values from the simulation output, with increasing growth rates as the shear is increased. The results are in even better agreement for the 800-, 600-, and 500-m runs (Figs. 12b–d). In all cases and for a given shear zone width, there is a nearly linear increase in average growth rate as the shear (hence, vorticity) is increased. The growth rates calculated from the simulations are slightly biased lower than the parametric model predictions, except in the 500-m runs that are

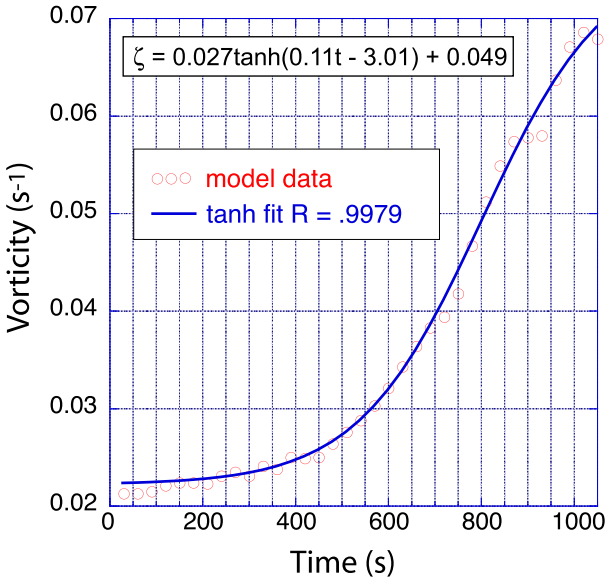

FIG. 11. Peak north–south-averaged vorticity as a function of time for the bc8m16s case (red circles) and tanh function fit (blue curve).

characterized by a slight high bias. It is hypothesized that the differences between the theoretical model and calculations decrease with decreasing width because wider shear zones can collapse to a greater degree than narrower shear zones before approaching the Nyquist grid limit on the resolution of frontal collapse. With few exceptions, there is a close agreement in the magnitude of the average growth rate between the parametric model and the calculations from the simulations.

The average growth rates across all baroclinic simulations are plotted as a function of the initial shear zone vorticity to convey the overall rate of growth in an aggregate sense (Fig. 13). There is a very good linear relationship between the average growth rate and the initial shear zone vorticity, both for the parametric model and for the simulation calculations. There is also a very good agreement between the parametric model and the simulation calculations. However, there is some spread due to the nature of the collapsing shear zone and the increase in averaged vorticity with time. That is, for a given initial vorticity, the average growth rates are larger for larger shear zone widths. Larger shear zone widths can collapse to a greater degree than smaller widths, thus, allowing for larger vorticity values at later times, hence, a larger average growth rate. For example, an initial vorticity of $0.02\,s^{-1}$ experiences growth rates of 0.0057, 0.0060, and 0.0063 for the 600-, 800-, and 1000-m cases, respectively.

e. *Emergence of discrete vortices*

As the simulations progress, instability leads to the emergence of discrete vortices as also noted in the barotropic cases simulated in BZ16. Since the baroclinic shear zones collapse and the vorticity within them increases, the growth rates are higher and discrete vortices emerge earlier than in the corresponding barotropic cases with the same initial shear zone width and shear magnitude (corresponding to the same initial vorticity) simulated in BZ16. By the time the vortices begin to emerge and the shear zone has fully collapsed, the shear zone vorticity has achieved its maximum value (e.g., the initial shear zone vorticity was $0.032\,s^{-1}$ and the vorticity within the emerging vortices is $\sim 0.07\,s^{-1}$, or more than double the initial value for the bc5m16s case).

Although the entire shear zone is characterized by upward vertical motions due to the pronounced secondary circulation associated with the zonal density gradient, localized regions of enhanced upward vertical velocity are nevertheless noted by 900–960 s in case bc5m16s (Figs. 14a,b). As the upward vertical velocity increases within localized regions, discrete regions of localized vertical vorticity maxima also emerge. By 1020 s (Fig. 14c), downdrafts have begun to form in the centers of most of the discrete vortices, although significant nonlinear evolution has already begun. The updrafts and downdrafts continue to intensify from 1080 through 1200 s (Figs. 14d–f) and achieve saturation after 1200 s (Fig. 14f). The remaining vortices that eventually begin to pair and coalesce into larger vortices (not shown) are generally characterized by central downdrafts flanked by updrafts between vortices.

TABLE 2. Parameters for the tanh function $\zeta = a\tanh(rt + m) + d$ in the various idealized baroclinic simulations and the time period the fit was performed. All cases are referred to via an acronym convention (e.g., case "bc8m20s," where "bc" denotes "baroclinic," "8m" denotes a shear zone width of 800 m, and "20s" denotes a $20\,m\,s^{-1}$ shear).

Simulation	a	r	m	d	Time period (s)
bc5m6s	−0.007 25	−0.2038	4.525	0.0208	120–1110
bc5m8s	−0.009 74	−0.2007	4.426	0.0275	210–1080
bc5m12s	0.013 87	0.2257	−4.491	0.0407	210–1050
bc5m16s	0.017 28	0.2578	−5.527	0.0533	210–870
bc5m20s	−0.017 47	−0.3538	7.228	0.062 26	330–840
bc5m24s	−0.023 50	−0.3137	6.620	0.078 03	210–780
bc6m8s	0.011 21	0.1657	−3.784	0.025 66	240–1080
bc6m12s	0.016 60	0.1702	−3.885	0.038 51	180–1080
bc6m16s	−0.020 62	−0.1929	4.319	0.050 16	210–1050
bc6m20s	0.022 46	0.2412	−5.219	0.059 85	120–960
bc6m24s	−0.027 13	−0.2278	4.927	0.071 63	60–840
bc8m12s	−0.018 72	−0.1243	3.246	0.035 64	180–1080
bc8m16s	0.027 41	0.1127	−3.019	0.049 24	120–1050
bc8m20s	0.031 75	0.1199	−3.145	0.059 69	150–1050
bc8m24s	0.034 67	0.1275	−3.236	0.068 16	90–1020
bc10m12s	0.027 52	0.066 83	−2.194	0.039 41	210–1230
bc10m16s	0.037 17	0.065 93	−2.177	0.052 94	180–1200
bc10m20s	0.037 73	0.075 86	−2.299	0.058 31	60–1050
bc10m24s	0.037 30	0.087 46	−2.245	0.062 84	60–1140

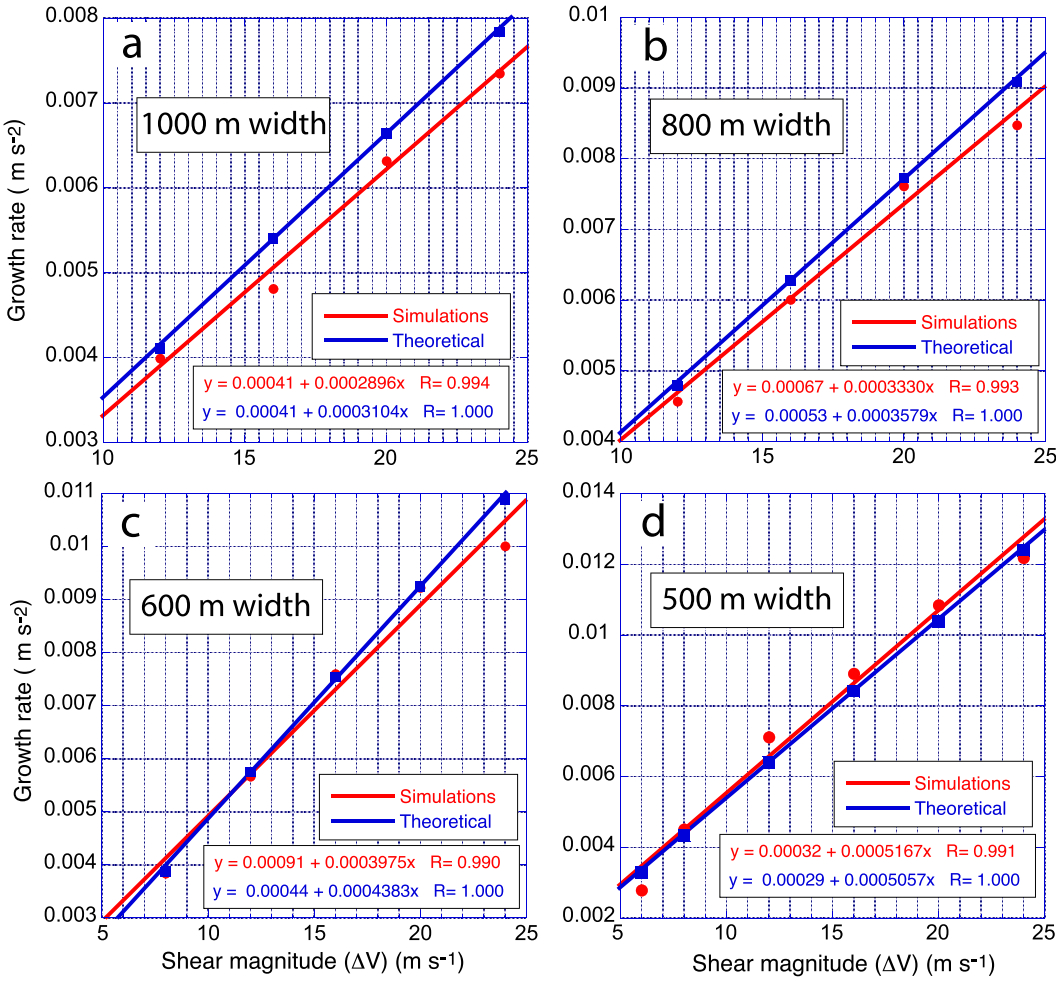

FIG. 12. Max average growth rates (red dots) plotted as a function of shear magnitude for four different shear zone widths. The max average growth rates as predicted by the parameterized growth rate in Eq. (4) and described in the text are denoted by blue dots. The red and blue lines indicate linear least squares fits to the respective data points. Also shown are the least squares linear fitting equations and the correlation coefficients of the fitted lines.

Compared to the nonlinear evolution of this case's barotropic counterpart (e.g., Figs. 11–12 in BZ16), several commonalities and differences exist. First, in the baroclinic case the vortices are spaced closer together than in the barotropic case. This is to be expected as the wavenumber of maximum growth increases (i.e., wavelength decreases) as the shear zone width collapses. Further, as the collapsing shear zone contains increasingly larger vorticity values, the growth rates are larger and the vortices emerge earlier and stronger in the baroclinic case. Also, there is much more variability in the spatial structure of the baroclinic vortices compared to the barotropic vortices. Whereas the barotropic vortices are all nearly the same shape and size, the baroclinic vortices take on a range of shapes and sizes. Also, although the emerging vortices go through some degree of nutation, it is less in the baroclinic case than in the barotropic case since the vortices tend to be more circular, and are perhaps somewhat constrained by the background east–west convergence within the shear zone. As in the barotropic case, there seems to be a wavenumber 2 modulation of the vorticity fields (i.e., as manifest as a structural resemblance in regions spaced 15 km apart in the periodic domain). Again as in the barotropic case, at later times there is generally a downdraft near the vortex center with flanking updrafts although the downdrafts seemed to be more centered in the baroclinic case (Fig. 14). Although the vertical velocity structure tends to be fairly symmetric in the barotropic case, in the baroclinic case there is a greater degree of spatial variability.

4. Discussion

All of the baroclinic simulations have a similar evolution. A region of constant vorticity bordered on the

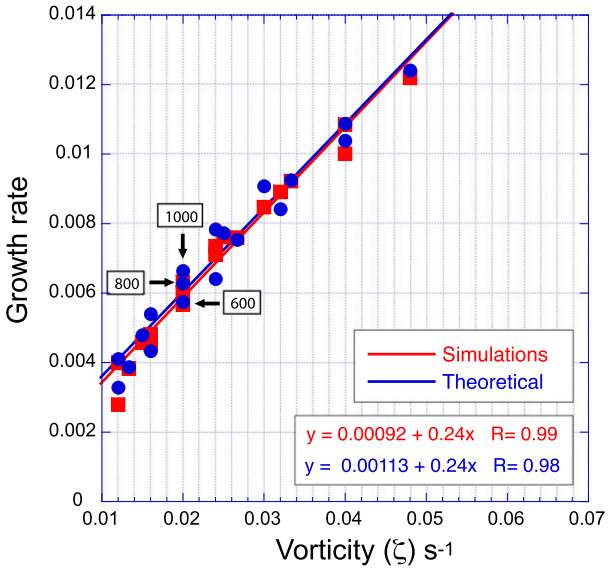

FIG. 13. Average max growth rates as a function of initial shear zone vorticity for all baroclinic simulations. Red squares represent simulation values, while blue circles are parameterized growth rate equation values.

east and west by regions of zero vorticity characterizes the initial state. Along the shear zone and below 1.5 km a vertically homogeneous east–west temperature gradient is imposed embedded in the shear zone. As the simulations spin up, the horizontal density gradient induces a secondary circulation. Therefore, the shear zone initially moves eastward before slowing and becoming nearly stationary. During this time, the shear zone undergoes collapse and the vorticity within the zone increases. It has been shown that the increase in vorticity is primarily due to stretching of vorticity, opposed slightly by tilting of the vertical vorticity by the secondary circulation. As the simulation spins up, the small random perturbations are initially damped. Eventually, as the initial perturbations have grown by about two orders of magnitude, wavelike features emerge along the shear zone. These wavelike features continue to amplify and eventually develop into discrete vortices.

a. Comparison with linear theory

For the baroclinic cases (as in the barotropic cases in BZ16), initially there is a spinup period wherein perturbations either do not grow exponentially or else are damped. After the initial spinup, a period of superexponential growth develops as the growth rates are increasing due to shear zone contraction. To extend the theoretical analytic results of linear theory applicable to the barotropic cases (BZ16) to the baroclinic cases, the analytic theory has been modified to allow for an evolving shear zone width. The modified parametric equation applied to the baroclinic simulations yields excellent agreement between the modified parametric model and "observed" growth rates from the simulations. The resulting growth rates are larger in the baroclinic cases than the barotropic cases (BZ16) for the same initial shear zone vorticity, since the growth rates are still a function of the vorticity, and the vorticity increases due to shear zone collapse. This result is consistent with McWilliams et al. (2009), who found that baroclinic frontogenesis enhanced the growth of 3D fluctuations along a simulated oceanic front. There is a high degree of correlation between the growth rates and the initial shear zone vorticity, with larger vorticity values leading to larger growth rates and earlier emergence of the wavelike structures and resultant discrete vortices.

Although some estimate of an initial shear zone vorticity and of the nature of the shear zone collapse could facilitate an estimate of the resulting growth rates in the baroclinic cases, this would seem to be more difficult to accomplish than in the barotropic cases (BZ16). In addition, once the wavelike structures and discrete vortices emerge in the baroclinic cases, they are farther along into the nonlinear regime and exhibit a more complicated structure than the barotropic cases. In the baroclinic cases, there is nothing to prevent the shear zone from continuing to collapse other than grid resolution. In all cases, the shear zones collapse to around twice the grid spacing before the emergence of the wavelike structures, and the resulting structures have wavelengths consistent with what would be predicted by a barotropic linear theory with a shear zone width of around 2–3Δ. Regardless of the actual resolution employed, it seems that the model will always try to collapse the gradient to around 2Δ. This tendency has also been shown in other simulations of frontal zones (e.g., Gall et al. 1987; Garner 1989). In nature, we find that actual boundaries (fronts, drylines, etc.) tend not to collapse to arbitrarily small scales. Eventually, turbulent diffusion would tend to limit the magnitudes of gradients across boundaries; however, there might be other processes that also limit these gradients (Hoskins 2003). For example, McWilliams and Molemaker (2011) suggest that growing frontal instabilities can actually have a frontolytic effect. Therefore, in nature, any collapsing shear zone would eventually tend toward the barotropic configurations of a nearly constant shear zone width even though the baroclinic simulations may initially be more appropriate.

b. Evolution of discrete vortices

The behavior of the vortices that develop in the baroclinic simulations is similar to those in the barotropic simulations (BZ16), with a few notable differences. In the baroclinic simulations, the emerging vortices are not

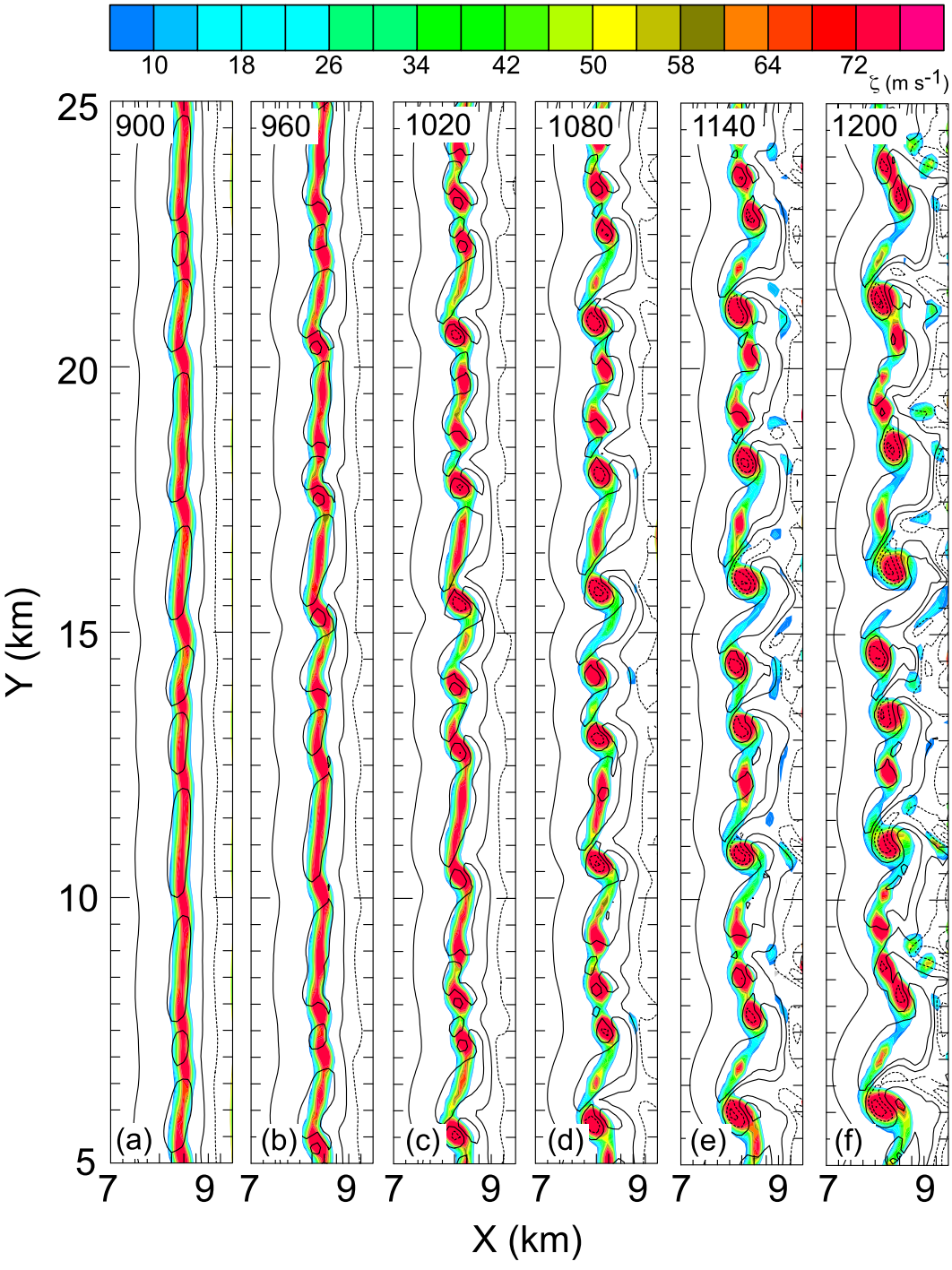

FIG. 14. Vertical vorticity (color filled) at $z = 550$ m for the bc5m16s case. The solid (dashed) black contours denoting positive (negative) vertical velocity at 2 m s^{-1} intervals starting at 1 (-1) m s^{-1}: (a) 900, (b) 960, (c) 1020, (d) 1080, (e) 1140, and (f) 1200 s.

as equally spaced, and have differing sizes compared to the barotropic cases. The results of LW97 also documented variability in the wavelengths and sizes of misocyclones that developed along a simulated outflow boundary. It is hypothesized that the greater degree of variability of the baroclinic simulations may be caused by the modulation of the most unstable wavenumber via nonlinear interactions with other less unstable wavenumbers (e.g., see additional

peaks in the spectral density estimates in Figs. 9–10). The simulated vortices in the present study also develop cores and connecting braids, although the latter structure is somewhat more complex than the simulated barotropic core-braid structure (BZ16). The present baroclinic vortex cores also rotate and nutate (although to a lesser degree than the barotropic vortices of BZ16), perhaps because the baroclinic vortices tend to be more circular than elliptical. As in the barotropic vortex cases, the vortices in the baroclinic cases eventually pair and merge at later times. Although it is beyond the scope of the present study to explore the vortex merger phenomenon in any detail, it is noted that misocyclone mergers have previously been reported by Marquis et al. (2007) along a dryline.

c. *Vertical motions in vortices*

Prior to the emergence of vortices, the baroclinic simulations are characterized by strong updrafts along the entire shear zone due to the secondary circulation associated with the density gradient within the zone. As the discrete vortices develop, stronger updrafts tend to develop between vortices, with downdrafts developing within the vortex cores. In contrast to the barotropic cases (BZ16), nearly every distinct vortex core in the baroclinic cases develops a central downdraft. These vertical motion characteristics are consistent with those found along a simulated baroclinic shear zone (LW97). Subjective analysis of several observational studies broadly conform to the updraft structure in the simulations: in particular, with generally strongest updrafts between or just north of vortex cores, weaker updrafts just south of vortex cores, and either the weakest updrafts or else downdrafts along the vortex core axis (e.g., Wilson et al. 1992; LW97; Kawashima and Fujiyoshi 2005; Arnott et al. 2006; Marquis et al. 2007; Campbell et al. 2014).

5. Conclusions

This study presents a series of idealized simulations that attempt to replicate the dynamics and evolution of shear zones typical of drylines and other near-surface boundaries to assess the possibility that the development of vortices with characteristic scales comparable to observed misocyclones is attributable to a baroclinically modified horizontal shearing instability (HSI) process. In many observed boundaries such as drylines and fronts, a horizontal density gradient exists across the shear zone. To see what effects a horizontal density gradient would have on the otherwise purely barotropic HSI mechanism, a series of baroclinic simulations have been performed. The series of 25 simulations are initialized with a north–south-oriented potential temperature gradient embedded within a constant-vorticity shear zone, employ north–south periodic boundary conditions, and have varying magnitudes of shear and differing shear zone widths (corresponding to differing initial vorticity and density gradient values).

The baroclinic simulations are similar to the barotropic simulations conducted by BZ16, with several notable differences. First, although the barotropic simulations feature a quasi-steady shear zone as the small initial perturbations are growing, the baroclinic simulations rapidly develop a secondary circulation due to the imposed horizontal density gradient. Convergence along the shear zone associated with the developing solenoidally forced secondary vertical circulation induces an accumulative shear zone contraction down to about twice the horizontal grid spacing of the simulation. The contracting shear zone width is accompanied by an increase in shear zone horizontal circulation and vertical vorticity, owing primarily to stretching though somewhat offset by tilting of the vertical vorticity into the horizontal by the secondary circulation.

Employing spectral estimates from the simulation output, comparison is made with barotropic simulations from a previous study (BZ16) and linear theory is extended to the baroclinic cases. The vertical vorticity increase due to the contracting shear zone leads to a larger growth rate for a given baroclinic run compared to its barotropic counterpart with the same initial shear zone width and shear magnitude. Additionally, contraction of the shear zone to scales barely resolvable by the grid resolutions leads to emerging vortices with much shorter wavelengths than the barotropic runs.

The new modified parametric model predicts a new growth rate for the collapsing shear zones, and is in excellent agreement with the growth rates computed from the simulations. This growth rate is dependent on the changing layer vorticity as opposed to the constant shear zone vorticity for barotropic shear zones (BZ16). Thus, for these idealized simulations, linear HSI theory can be adequately extended to the baroclinic cases to explain the growth of small perturbations to form mature misocyclonic vortices at observed dryline scales in the presence of horizontal density gradients.

Although it is well understood why the baroclinic simulations tend to collapse frontal zones down to minimally resolvable scale (especially in this case with a free-slip lower boundary condition and no friction), real atmospheric boundaries do not collapse down in scale beyond some point. Because of turbulence or other mechanisms, real boundaries that are collapsing would hypothetically achieve an approximately steady-state

finite width. Therefore, it is hypothesized that aspects of both barotropic and baroclinic HSI may describe instabilities along real boundaries at various stages of their individual evolutions.

Acknowledgments. The lead author gratefully acknowledges helpful discussions with committee members Drs. Michael Biggerstaff, Alan Shapiro, Evgeni Fedorovich, Louis Wicker, S. Lakshmivarahan, and his advisor (CLZ) during the preparation of his Ph.D. dissertation at the University of Oklahoma (a portion of which the present study reports). Edward Mansell and Alison Silveira are also gratefully acknowledged for assistance with COMMAS code. Major funding for the current project was provided under National Science Foundation Grants AGS-0130316, AGS-0638572, and AGS-1063537 and by the NOAA/National Severe Storms Laboratory. Funding was also provided by NOAA/Office of Oceanic and Atmospheric Research under NOAA–University of Oklahoma Cooperative Agreement NA11OAR4320072, U.S. Department of Commerce.

REFERENCES

Arnott, N. R., Y. P. Richardson, J. M. Wurman, and E. M. Rasmussen, 2006: Relationship between a weakening cold front, misocyclones, and cloud development on 10 June 2002 during IHOP. *Mon. Wea. Rev.*, **134**, 311–335, doi:10.1175/MWR3065.1.

Atkins, N. T., R. M. Wakimoto, and T. M. Weckwerth, 1995: Observations of the sea-breeze front during CaPE. Part II: Dual-Doppler and aircraft analysis. *Mon. Wea. Rev.*, **123**, 944–969, doi:10.1175/1520-0493(1995)123<0944:OOTSBF>2.0.CO;2.

Buban, M. S., 2014: The formation of small-scale atmospheric vortices via horizontal shearing instability. Ph.D. dissertation, University of Oklahoma, 215 pp. [Available online at http://hdl.handle.net/11244/13870.]

——, and C. L. Ziegler, 2016: The formation of small-scale atmospheric vortices via horizontal shearing instability. *J. Atmos. Sci.*, **73**, 2061–2084, doi:10.1175/JAS-D-14-0355.1.

——, ——, E. N. Rasmussen, and Y. P. Richardson, 2007: The dryline on 22 May 2002 during IHOP: Ground radar and in situ data analyses of the dryline and boundary layer evolution. *Mon. Wea. Rev.*, **135**, 2473–2505, doi:10.1175/MWR3453.1.

——, ——, E. R. Mansell, and Y. P. Richardson, 2012: Simulation of dryline misovortex dynamics and cumulus formation. *Mon. Wea. Rev.*, **140**, 3525–3551, doi:10.1175/MWR-D-11-00189.1.

Campbell, P. C., B. Geerts, and P. T. Bergmaier, 2014: A dryline in southeast Wyoming. Part I: Multiscale analysis using observations and modeling on 22 June 2010. *Mon. Wea. Rev.*, **142**, 268–289, doi:10.1175/MWR-D-13-00049.1.

Coniglio, M. C., D. J. Stensrud, and L. J. Wicker, 2006: Effects of upper-level shear on the structure and maintenance of strong quasi-linear mesoscale convective systems. *J. Atmos. Sci.*, **63**, 1231–1252, doi:10.1175/JAS3681.1.

Crook, N. A., T. L. Clark, and M. W. Moncrieff, 1991: The Denver cyclone. Part II: Interaction with the convective boundary layer. *J. Atmos. Sci.*, **48**, 2109–2126, doi:10.1175/1520-0469(1991)048<2109:TDCPII>2.0.CO;2.

Friedrich, K., D. E. Kingsmill, and C. R. Young, 2005: Misocyclone characteristics along Florida gust fronts during CaPE. *Mon. Wea. Rev.*, **133**, 3345–3367, doi:10.1175/MWR3040.1.

Gall, R. L., R. T. Williams, and T. L. Clark, 1987: On the minimum scale of fronts. *J. Atmos. Sci.*, **44**, 2562–2574, doi:10.1175/1520-0469(1987)044<2562:OTMSOS>2.0.CO;2.

Garner, S. T., 1989: Fully Lagrangian numerical solutions of unbalanced frontogenesis and frontal collapse. *J. Atmos. Sci.*, **46**, 717–739, doi:10.1175/1520-0469(1989)046<0717:FLNSOU>2.0.CO;2.

Hoskins, B. J., 2003: Back to frontogenesis. *A Half Century of Progress in Meteorology: A Tribute to Richard Reed, Meteor. Monogr.*, No. 31, Amer. Meteor. Soc., 49–60, doi:10.1175/0065-9401-31.53.49.

Jenkins, G. M., and D. G. Watts, 1969: *Spectral Analysis and Its Applications*. Holden-Day, 525 pp.

Kawashima, M., 2011: Numerical study of horizontal shear instability waves along narrow cold frontal rainbands. *J. Atmos. Sci.*, **68**, 878–903, doi:10.1175/2010JAS3599.1.

——, and Y. Fujiyoshi, 2005: Shear instability wave along a snowband: Instability structure, evolution, and energetics derived from dual-Doppler radar data. *J. Atmos. Sci.*, **62**, 351–370, doi:10.1175/JAS-3392.1.

Klemp, J. B., and R. B. Wilhelmson, 1978: The simulation of three-dimensional convective storm dynamics. *J. Atmos. Sci.*, **35**, 1070–1096, doi:10.1175/1520-0469(1978)035<1070:TSOTDC>2.0.CO;2.

Lee, B. D., and R. B. Wilhelmson, 1997: The numerical simulation of non-supercell tornadogenesis. Part I: Initiation and evolution of pretornadic misocyclone circulations along a dry outflow boundary. *J. Atmos. Sci.*, **54**, 32–60, doi:10.1175/1520-0469(1997)054<0032:TNSONS>2.0.CO;2.

Mansell, E. R., C. L. Ziegler, and E. C. Bruning, 2010: Simulated electrification of a small thunderstorm with two-moment bulk microphysics. *J. Atmos. Sci.*, **67**, 171–194, doi:10.1175/2009JAS2965.1.

Marquis, J., Y. P. Richardson, and J. M. Wurman, 2007: Kinematic observations of misocyclones along boundaries during IHOP. *Mon. Wea. Rev.*, **135**, 1749–1768, doi:10.1175/MWR3367.1.

McWilliams, J. C., and M. J. Molemaker, 2011: Baroclinic frontal arrest: A sequal to unstable frontogenesis. *J. Phys. Oceanogr.*, **41**, 601–619, doi:10.1175/2010JPO4493.1.

——, ——, and E. I. Olafsdottir, 2009: Linear fluctuation growth during frontogenesis. *J. Phys. Oceanogr.*, **39**, 3111–3129, doi:10.1175/2009JPO4186.1.

Miao, Q., and B. Geerts, 2007: Finescale vertical structure and dynamics of some dryline boundaries observed in IHOP. *Mon. Wea. Rev.*, **135**, 4161–4184, doi:10.1175/2007MWR1982.1.

Murphey, H. V., R. M. Wakimoto, C. Flamant, and D. E. Kingsmill, 2006: Dryline on 19 June 2002 during IHOP. Part I: Airborne Doppler and LEANDRE II analyses of the thin line structure and convection initiation. *Mon. Wea. Rev.*, **134**, 406–430, doi:10.1175/MWR3063.1.

Peckham, S. E., and L. J. Wicker, 2000: The influence of topography and lower-tropospheric winds on dryline morphology. *Mon. Wea. Rev.*, **128**, 2165–2189, doi:10.1175/1520-0493(2000)128<2165:TIOTAL>2.0.CO;2.

Pietrycha, A. E., and E. N. Rasmussen, 2004: Finescale surface observations of the dryline: A mobile mesonet perspective. *Wea. Forecasting*, **19**, 1075–1088, doi:10.1175/819.1.

Rayleigh, L., 1879: On the stability, or instability, of certain fluid motions. *Proc. London Math. Soc.*, **S1-11**, 57–72, doi:10.1112/plms/s1-11.1.57.

Wicker, L. J., and R. B. Wilhelmson, 1995: Simulation and analysis of tornado development and decay within a three-dimensional supercell thunderstorm. *J. Atmos. Sci.*, **52**, 2675–2703, doi:10.1175/1520-0469(1995)052<2675:SAAOTD>2.0.CO;2.

——, and W. Skamarock, 2002: Time-splitting methods for elastic models using forward time schemes. *Mon. Wea. Rev.*, **130**, 2088–2097, doi:10.1175/1520-0493(2002)130<2088:TSMFEM>2.0.CO;2.

Wilson, J. W., G. B. Foote, N. A. Crook, J. C. Frankhauser, C. G. Wade, J. D. Tuttle, C. K. Mueller, and S. K. Kruger, 1992: The role of boundary-layer convergence zones and horizontal rolls in the initiation of thunderstorms: A case study. *Mon. Wea. Rev.*, **120**, 1785–1815, doi:10.1175/1520-0493(1992)120<1785:TROBLC>2.0.CO;2.

Ziegler, C. L., and C. E. Hane, 1993: An observational study of the dryline. *Mon. Wea. Rev.*, **121**, 1134–1151, doi:10.1175/1520-0493(1993)121<1134:AOSOTD>2.0.CO;2.

——, W. J. Martin, R. A. Pielke, and R. L. Walko, 1995: A modeling study of the dryline. *J. Atmos. Sci.*, **52**, 263–285, doi:10.1175/1520-0469(1995)052<0263:AMSOTD>2.0.CO;2.

——, E. N. Rasmussen, M. S. Buban, Y. P. Richardson, L. J. Miller, and R. M. Rabin, 2007: The ''Triple Point'' on 24 May 2002 during IHOP. Part II: Ground-radar and in situ boundary layer analysis of cumulus development and convection initiation. *Mon. Wea. Rev.*, **135**, 2443–2472, doi:10.1175/MWR3411.1.

——, E. R. Mansell, J. M. Straka, D. R. MacGorman, and D. W. Burgess, 2010: The impact of spatial variations of low-level stability on the life cycle of a simulated supercell storm. *Mon. Wea. Rev.*, **138**, 1738–1766, doi:10.1175/2009MWR3010.1.